



Block and sub-block boundary strengthening in lath martensite



C. Du, J.P.M. Hoefnagels*, R. Vaes, M.G.D. Geers

Department of Mechanical Engineering, Eindhoven University of Technology, P.O. Box 513, 5600 MB Eindhoven, The Netherlands

ARTICLE INFO

Article history:

Received 25 November 2015

Received in revised form 28 January 2016

Accepted 29 January 2016

Available online xxxx

Keywords:

Lath martensite

Boundaries

Strengthening mechanism

Uniaxial micro-tensile test

ABSTRACT

Well-defined uniaxial micro-tensile tests were performed on lath martensite single block specimens and multi-block specimens with different numbers of block boundaries parallel to the loading direction. Detailed slip trace analyses consistently revealed that the $\{110\}<111>$ slip system with the highest Schmid factor is activated. Both block and sub-block boundaries act as barriers to dislocation motion, whereby a Hall–Petch like behavior is observed. Sub-block boundary strengthening appears to be only slightly less effective than block boundary strengthening, even though fracture analyses indicate that dislocation motion can cross sub-block boundaries, but not block boundaries.

© 2016 Elsevier Ltd. All rights reserved.

Lath martensite, the most typical morphology of martensite, has high industrial relevance being the prime constituent that elevates the strength in high strength steels, such as dual-phase steel, transformation-induced plasticity steel and quenching-partitioning steel. For decades, research has been conducted on the strengthening mechanisms of this material, which can be categorized into (i) forest dislocation hardening [1,2], (ii) solid solution hardening by alloying elements [2], (iii) precipitation strengthening, e.g., by carbides [2,3], and most importantly (iv) substructure boundary strengthening [4–11]. Indeed, the hierarchical structure, which shows substructures of packets, blocks and sub-blocks within prior austenite grains, gives lath martensite an abundance of internal boundaries [12]. It was suggested that these boundaries can act as potential barriers to dislocation motion [2,4,5,6].

The mechanical effect of lath martensite boundaries has been investigated in a number of high quality research studies, which can be categorized according to the experimental methodologies used: Morito et al. and Zhang et al. performed macroscopic tensile tests and concluded that a Hall–Petch relation holds between the yield strength and the averaged block size [4,5]. A more microscopic analysis was carried out by Ohmura et al. through nano- and micro-indentation tests, who concluded that the block structure increases the hardness of martensite [3,6], although no differentiation was made between different types of (packet/block/sub-block) boundaries. Shibata et al. [7,8] performed micro-bending tests, including two single-block specimen tests. From slip trace analysis from the bending side, where the slip activity is highly inhomogeneous due to the complex loading state, they concluded that the block boundaries are the most effective

barriers to dislocation motion. The influence of the sub-block boundaries' presence was, however, not investigated in detail. Alternatively, lath martensite has been tested by micro-pillar compression tests, including TEM diffraction analysis, by Ghassemi-Armaki et al. [9,10], who found that single block specimens show perfect elasto-plastic behavior, whereas multiple block specimens show significant strain hardening. These authors acknowledge, however, that the multiple-block specimens may be jeopardized with one or more packet boundaries, making it difficult to determine whether the hardening is due to the block or packet boundaries. Finally, micro-tension tests on lath martensite, including (single-sided) electron-backscattered diffraction (EBSD) analysis, were conducted by Mine et al. [11]. Besides specimens containing multiple packets and even multiple prior austenite grains, also two single-packet specimens were tested with the block boundaries parallel to the loading direction. The authors concluded that block boundaries can be an effective strengthening mechanism, although the contribution of the sub-block boundaries was again not studied. In general, the distinct role of block and sub-block boundaries in terms of the resulting strengthening mechanism remains to be unclear. Therefore, to directly expose the most relevant microscopic deformation mechanisms, reliable experiments under well-defined loading conditions are required, testing single-packet specimens with different numbers of block boundaries as well as single-block specimens with different numbers of sub-block boundaries. The mechanical tests should be accompanied by detailed orientation analyses from at least two sides to confirm the 3D orientation(s) throughout the specimen volume.

In this study, we perform uniaxial micro-tensile tests, using an in-house developed nano-force tensile tester (Fig. 1(a, b)) [13], of lath martensite specimens consisting of either a single packet or a single block with a range of block or sub-block boundaries respectively. The

* Corresponding author.

E-mail address: j.p.m.hoefnagels@tue.nl (J.P.M. Hoefnagels).

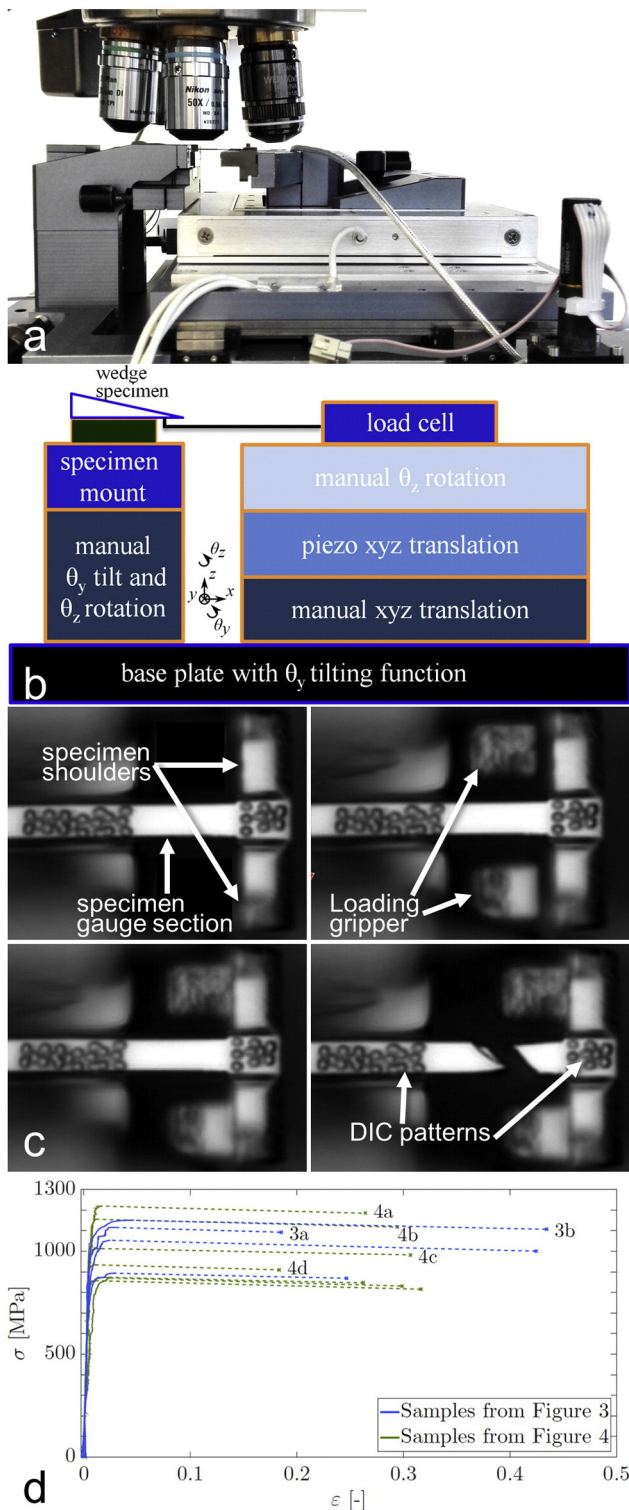


Fig. 1. (a) The in-house developed nano-force tensile stage under an optical profilometer. (b) Schematic drawing of the tensile stage. (c) The testing procedure, in which the load is applied by a 'double-hook' gripper on the specimen shoulders (only the specimen gauge section is in focus). (d) Stress–strain curves of all specimens shown in Figs. 3 and 4; the specimens discussed in detail are labeled with their figure numbers. Note that in the unstable deformation regime (dashed line) the applied load decreases slightly.

methodology involves the following steps: (i) fabrication of a wedge of lath martensite by grinding/polishing/electro-chemical etching, (ii) careful selection of the specimen location at the edge of wedge based on EBSD maps, (iii) focused ion beam milling of micro-tensile

specimens with constant thickness, (iv) detailed top- and bottom-side EBSD analysis of each specimen (Figs. 2, 3, 4), (v) uniaxial tensile tests with highly accurate specimen alignment, force- and displacement measurements (Fig. 1(a, b, c)) under (vi) in-situ optical microscopy enabling microscopic slip trace analysis [14]. We will show that not only block boundaries but also sub-block boundaries play a key role in lath martensite strengthening.

Bulk lath martensite (0.092C–1.68Mn–0.24Si–0.57Cr) out of which the micro-tensile specimens are made was heat treated by homogenization at austenite temperature (first batch, 950 °C for 30 min; second batch, 1000 °C for 120 min), followed by water quenching. Most specimens were discarded for analysis because detailed EBSD analysis at both specimen sides showed that the microstructure was not homogeneous over the thickness. For a first batch of specimens, with an average block size smaller than the specimen size, only one specimen was identified with the intended microstructure and desired orientation. Therefore, a second batch of specimens with larger block size was produced with more suitable specimens. The single specimen retained from the first batch is first discussed, since it clearly reveals the role of the block boundary, see Fig. 2.

The EBSD maps of the top and bottom sides (Fig. 2(a, b)) confirm that the block boundary is approximately in the middle of the specimen and runs vertically through the thickness. The pole figures of the top and bottom sides are shown in Fig. 2(e, f), which demonstrate the uniformity of the microstructure within the specimens. The block boundary was confirmed to be a high angle boundary with ~60 degree misorientation. From the austenite-to-martensite orientation relationship it is known that boundaries inside packets form at a {111} prior austenite plane, i.e. parallel to a {110} martensite plane, therefore, the dots (red circles) on the peripheral in the {110} plots in Fig. 2(e, f) confirm that the block boundary is perpendicular to the specimen surface. Black circles highlight the favorable slip direction and slip plane of the {110}<111> slip systems. The marked slip traces (dotted lines) in Fig. 2(d) is in good agreement with the favorable slip systems, considering the significant crystal rotation upon fracture. More convincing evidence for single slip system activation is shown below for the single block specimens. Interestingly, the fracture surfaces join exactly at the block boundary in the middle, where the slip systems are interrupted. This is the first direct evidence that block boundaries in lath martensite act as barriers to dislocation motion for the case where the activated slip system is crossed by a block boundary.

From the second batch of specimens, a series of specimens with different configurations of boundaries are produced and tested: specimens with no block boundaries (i.e. single block specimens), 1 parallel block boundary and multiple parallel block boundaries. In Fig. 3(a, b), two examples of specimens with multiple block boundaries are shown. In the case of few block boundaries (Fig. 3(a)), with large boundary-free regions at the specimen sides, the fracture propagates from both specimen sides and arrests at the first block boundary, similar to the single block boundary case. However, between the two block boundaries, the slip activity is more complex due to the induced loading constraints, resulting in a jagged fracture surface. The same phenomenon is also observed when the boundary-free regions at the specimen sides are small, due to the presence of many block boundaries (Fig. 3(b)). Due to the fact that the dislocations cannot propagate through block boundaries, a zig-zag fracture surface is formed with multiple peaks, again in agreement with the block boundaries. The identified slip systems of both samples are in line with the ones marked with corresponding colors of the blocks in the pole figures (Fig. 3(c, d)).

To analyze the strengthening caused by block boundaries, Fig. 3(e) shows the critical stress, $\tau_{critical}$, versus the square root of the average number of block boundaries, \sqrt{m} where m is the average number of block boundaries observed at both sides. $\tau_{critical}$ is calculated by multiplying the highest Schmid factor of the largest block with the tensile strength, which is used as some specimens localize before 2% strain offset.

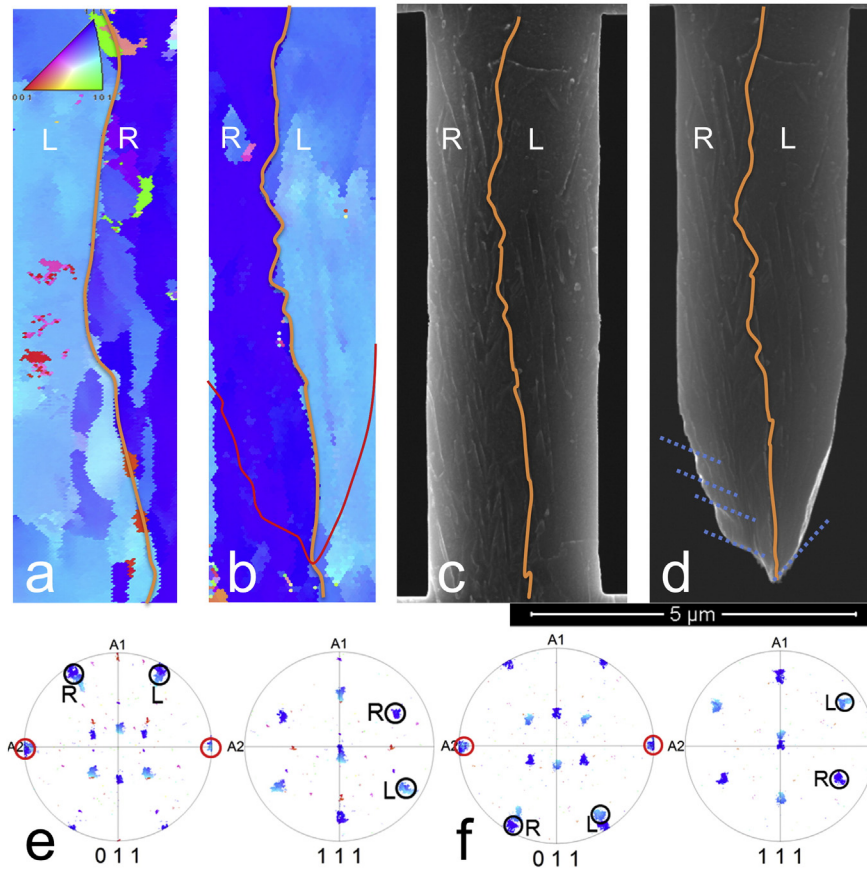


Fig. 2. EBSD maps of a bi-block specimen from front (a) and backside (b). Backside SEM image before (c) and after (d) fracture. (e, f) The $\{110\}$ and $\{111\}$ pole figures of the front side and backside respectively. The circles indicate the observed slip systems of both the left block (L) and the right block (R). (For interpretation of the references to color in this figure legend, the reader is referred to the web version of this article.)

Interestingly, Fig. 3(e) shows that $\tau_{critical}$ increases linearly with \sqrt{m} . This linear relationship provides microscopic evidence of a Hall–Petch type relationship for block boundaries, as already suggested in [4,5]. Note that only clean multi-block specimens have been included in Fig. 3(e), i.e. all of these specimens are free of sub-block boundaries, except for the specimen with the lowest $\tau_{critical}$ where one sub-block boundary is observed only on the top-right side. This specimen would have had an even lower $\tau_{critical}$ without this sub-block boundary. Therefore, the observed strengthening cannot be attributed to the presence of sub-block boundaries, but must be caused by the block boundaries. The slope of the linear fit in Fig. 3(e) is 132 [MPa], including all inaccuracies. This value cannot directly be compared to Hall–Petch constants for bulk lath martensite, because the fraction of ‘grains’ in our micro-specimens that are cut off at the side by the free surface is significant.

Next, the strengthening effect of sub-block boundaries is investigated. Two examples of single block specimens from the same packet and with the same sub-blocks are shown in Fig. 4(a, b). The misorientation between the sub-blocks is $\sim 8^\circ$, i.e. a small angle boundary. Both fracture surfaces and slip traces are continuous across the sub-block boundary and no difference can be observed in the two sub-blocks due to the small misorientation. Both samples in Fig. 4(a, b) reveal the same slip trace and fracture surface, which demonstrates the reproducibility of this testing method as well as the consistent activation of micro-mechanical mechanisms. The $\{110\}$ – $\langle 111 \rangle$ system with the highest Schmid factor is activated in both sub-blocks and marked with black circles in the pole figures.

Two other single block specimens are shown in Fig. 4(c) and (d). Again, analysis shows that the slip system of the $\{110\}$ – $\langle 111 \rangle$ family with the highest Schmid factor is again active. The slip traces are nearly equivalent in the two sub-blocks, while the fracture surfaces cross the

sub-block boundaries. The specimen in Fig. 4(d) contains more sub-block boundaries in the upper part. Perhaps not surprisingly, the specimen fractures at the bottom part where it is less heterogeneous, which confirms the sub-block boundary strengthening mechanism.

For the single block specimens, $\tau_{critical}$ is plotted as a function of the square root of the number of sub-block boundaries, n , in Fig. 4(e), where n is calculated similarly to m in Fig. 3(e). The main difference between the four specimens shown in Fig. 4 lies in the number of sub-block boundaries crossed by the fracture surface. The more sub-block boundaries crossed by the fracture surface, the stronger the specimen are. Similar to the strengthening mechanism of block boundaries, $\tau_{critical}$ increases linearly with \sqrt{n} , with a slope of 90 MPa, which suggests a Hall–Petch type relationship also for sub-block boundary strengthening. Although the slopes of Figs. 3(e) and 4(e) are subject to experimental and microstructural uncertainties, the slightly smaller slope in Fig. 4(e) indicates that strengthening by sub-block boundaries is only somewhat less effective. This in-depth uniaxial tension analysis directly proves that the strengthening effect of sub-block boundaries is highly important, which is in sharp contrast to the statement in Ref. [7] that the sub-block boundaries have a negligible contribution to the macroscopic strength of lath martensite.

Interestingly, yet qualitative, in-situ TEM observations in [15] showed that dislocations pile up at a low angle boundary followed by transmission through it. This may explain why (almost) all fracture surfaces of the single-block specimens show a single straight fracture surface spanning the complete cross-section. It was also suggested in [15], from the sudden disappearance of dislocations at a block boundary, that dislocations ‘reflect’ and then glide along the high-angle boundaries (to the free surface). If dislocations can indeed glide along a block boundary instead of cutting through the boundary, this may explain

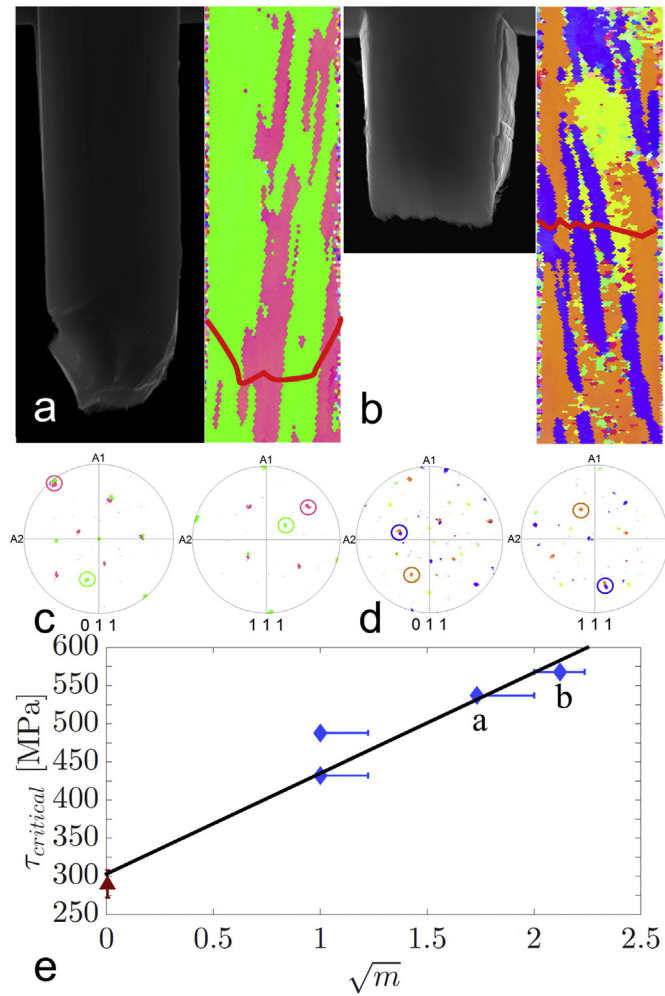
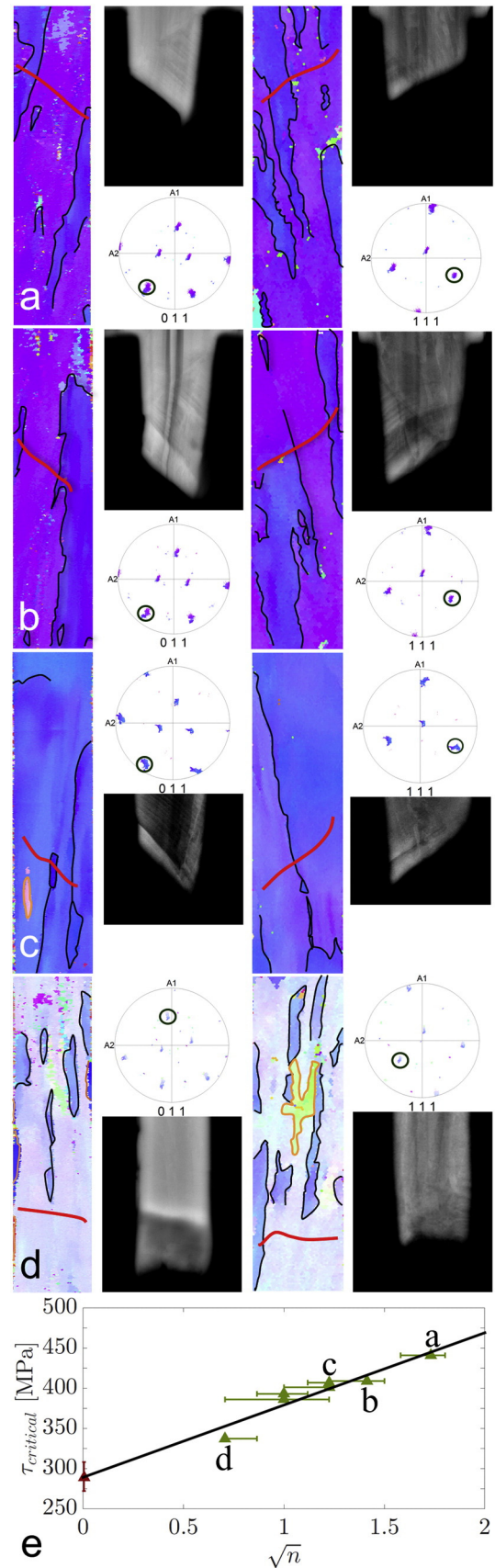


Fig. 3. (a, b) The fracture surface (left) and EBSD map (right) for both specimens marked in (e). The length of undeformed samples is 9 μm . Red curves mark the fracture traces in the EBSD maps. (c, d), {110} and {111} pole figures of samples a and b respectively, (e) $\tau_{critical}$ versus \sqrt{m} , where the error bars reflect (an estimation of) the uncertainty in the number of block boundaries m (same for n in Fig. 4(e)). The data point at $\sqrt{m} = 0$ in red corresponds to the strength without block and sub-block boundaries as obtained from the offset in Fig. 4(e). (For interpretation of the references to color in this figure legend, the reader is referred to the web version of this article.)

why the fracture surfaces of two adjacent blocks join exactly at the block boundary, as shown most clearly in Fig. 2, and why the fracture surface for multi-block specimens is jagged.

In summary, uniaxial micro-tensile tests were performed on lath martensite specimens with different numbers of block boundaries parallel to the loading direction and single-block specimens with different numbers of sub-block boundaries. For the single-block specimens, the observed slip traces match the slip system with the highest Schmid factor. Both the block and sub-block boundaries act as a barrier for dislocation motion, clearly strengthening the material. A Hall–Petch type relationship was found between $\tau_{critical}$ and the number of boundaries, and the strengthening effect of sub-block boundaries appears to be only slightly less effective as that of block boundaries. For multi-block specimens, the fracture surface joins at the block boundary,

Fig. 4. (a–d) EBSD maps and BSE fracture images of the front (left) and back (right) side and the {110} and {111} pole figures for each specimen, marked in (e). The length of undeformed samples is 9 μm . (e) $\tau_{critical}$ versus the square root of number of sub-block boundaries \sqrt{n} . The fracture traces and sub-block boundaries are marked with, respectively, red and black curves in the EBSD maps. (For interpretation of the references to color in this figure legend, the reader is referred to the web version of this article.)



indicating that the fracture cannot propagate across block boundaries. This is in contrast to sub-block boundaries for which a single straight fracture surface over the cross-section is consistently identified.

Acknowledgments

This research was carried out under project number M22.2.11424 in the framework of the Research Program of the Materials innovation institute (M2i) (www.m2i.nl).

References

- [1] S. Takaki, K. Ngo-huynh, N. Nakada, T. Tsuchiyama, *ISIJ Int.* 52 (2012) 710–716.
- [2] G. Krauss, *Mater. Sci. Eng. A* 273–275 (1999) 40–57.
- [3] T. Ohmura, T. Hara, K. Tsuzaki, *Scr. Mater.* 49 (2003) 1157–1162.
- [4] S. Morito, H. Yoshida, T. Maki, X. Huang, *Mater. Sci. Eng. A* 438–440 (2006) 237–240.
- [5] C. Zhang, Q. Wang, J. Ren, R. Li, M. Wang, F. Zhang, K. Sun, *Mater. Sci. Eng. A* 534 (2012) 339–346.
- [6] T. Ohmura, T. Hara, K. Tsuzaki, *J. Mater. Res.* 18 (2003) 1465–1470.
- [7] A. Shibata, T. Nagoshi, M. Sone, S. Morito, Y. Higo, *Mater. Sci. Eng. A* 527 (2010) 7538–7544.
- [8] A. Shibata, T. Nagoshi, M. Sone, S. Morito, Y. Higo, *J. Alloys Compd.* 577 (2013) S555–S558.
- [9] H. Ghassemi-Armaki, P. Chen, S. Bhat, S. Sadagopan, S. Kumar, A. Bower, *Acta Mater.* 61 (2013) 3640–3652.
- [10] H. Ghassemi-Armaki, R. Maass, S.P. Bhat, S. Sriram, J.R. Greer, K.S. Kumar, *Acta Mater.* 62 (2014) 197–211.
- [11] Y. Mine, K. Hirashita, H. Takashima, M. Matsuda, K. Takashima, *Mater. Sci. Eng. A* 560 (2013) 535–544.
- [12] S. Morito, H. Tanaka, R. Konishi, T. Furuhashi, T. Maki, *Acta Mater.* 51 (2003) 1789–1799.
- [13] L.J. Bergers, J.P.M. Hoefnagels, M.G.D. Geers, *J. Phys. D: Appl. Phys.* 47 (2014) 495306.
- [14] C. Du, J.P.M. Hoefnagels, L.J. Bergers, M.G.D. Geers, (submitted for publication) 2016.
- [15] T. Ohmura, A.M. Minor, E.A. Stach, J.W. Morris, *J. Mater. Res.* 19 (2004) 3626–3632.